

Scanning tunneling spectroscopy as a probe of multi- \mathbf{Q} magnetic states of itinerant magnets

Maria N. Gastiasoro,¹ Ilya Eremin,² Rafael M. Fernandes,³ and Brian M. Andersen¹

¹*Niels Bohr Institute, University of Copenhagen,
Universitetsparken 5, DK-2100 Copenhagen, Denmark*

²*Institut für Theoretische Physik III, Ruhr-Universität Bochum, 44801 Bochum, Germany*

³*School of Physics and Astronomy, University of Minnesota, Minneapolis, Minnesota 55455, USA*

The combination of electronic correlations and Fermi surfaces with multiple nesting vectors can lead to the appearance of complex multi- \mathbf{Q} magnetic ground states, hosting unusual states such as chiral density-waves and quantum Hall insulators. Distinguishing single- \mathbf{Q} and multi- \mathbf{Q} magnetic phases is however a notoriously difficult experimental problem. Here we propose theoretically that the local density of states (LDOS) near a magnetic impurity, whose orientation may be controlled by an external magnetic field, can be used to map out the detailed magnetic configuration of an itinerant system and distinguish unambiguously between single- \mathbf{Q} and multi- \mathbf{Q} phases. We demonstrate this concept by computing and contrasting the LDOS near a magnetic impurity embedded in three different magnetic ground states relevant to iron-based superconductors – one single- \mathbf{Q} and two double- \mathbf{Q} phases. Our results open a promising avenue to investigate complex magnetic configurations in itinerant systems via standard scanning tunneling spectroscopy (STS), without requiring spin-resolved capability.

Despite its predominance in localized spin systems^{1,2}, magnetic frustration is also found in several itinerant systems. While in most cases magnetic frustration can arise due to the geometry of the lattice or competing exchange interactions, in purely itinerant systems it can be manifested as a degeneracy among different nesting-driven magnetic instabilities with symmetry-related ordering vectors \mathbf{Q} ³. Depending on the symmetry of the lattice and on the topology of the Fermi surface, different sets of \mathbf{Q} vectors are possible⁴. In a square lattice, a compensated metal with small hole-like and electron-like Fermi pockets, as shown in Fig. 1(a), has magnetic instabilities at the two nesting vectors $\mathbf{Q}_1 = (\pi, 0)$ and $\mathbf{Q}_2 = (0, \pi)$, which are related by a 90° rotation. The resulting double- \mathbf{Q} phases have been shown to also display charge and vector-chirality orders⁵. Such a toy model has been widely employed to study the magnetic properties of iron-based superconductors^{6,7} and, more recently, of topological Kondo insulators⁸. In the triangular and honeycomb lattices with a hexagonal Fermi surface, as shown in Fig. 1(b), three nesting vectors related by 60° rotations are present, $\mathbf{Q}_1 = (0, \frac{2\pi}{\sqrt{3}})$, $\mathbf{Q}_2 = (\frac{\pi}{3}, -\frac{\pi}{\sqrt{3}})$, and $\mathbf{Q}_3 = (-\frac{\pi}{3}, -\frac{\pi}{\sqrt{3}})$. Interestingly, the possible triple- \mathbf{Q} states display semi-metallic and quantum Hall insulator behaviors. Such a model has been employed to study doped cobaltates and graphene doped to the van Hove singularity point of its band structure^{9–12}. Magnetic instabilities of single- versus triple- \mathbf{Q} phases of hexagonal Fermi surface were also studied recently in the context of topological insulators forming magnetic skyrmionic ground state configurations¹³. In all cases, the presence of repulsive electronic interactions is essential to stabilize the magnetic instabilities over other density-wave or superconducting instabilities.

In spite of the interesting properties of multi- \mathbf{Q} phases,

unambiguously establishing their existence in a material is a notoriously difficult experimental problem. For instance, neutron scattering, which is the prime tool to probe magnetic configurations, is sensitive not only to the intensity of the order parameters, but also to their corresponding volume fraction. As such, the neutron scattering signatures of a multi- \mathbf{Q} phase can be nearly indistinguishable from the signatures of multiple domains of different single- \mathbf{Q} phases. This general issue has been previously highlighted in the literature in the context of a variety of different materials^{14–17}. In some cases, the fact that single- \mathbf{Q} or multi- \mathbf{Q} states break additional discrete symmetries of the lattice may facilitate their experimental distinction. However, in many cases this distortion may be too small to be resolved experimentally. Several other bulk probes, such as angle-resolved photo-emission spectroscopy (ARPES), suffer from similar issues.

This analysis begs the question of whether local probes may be more appropriate to distinguish single- \mathbf{Q} versus

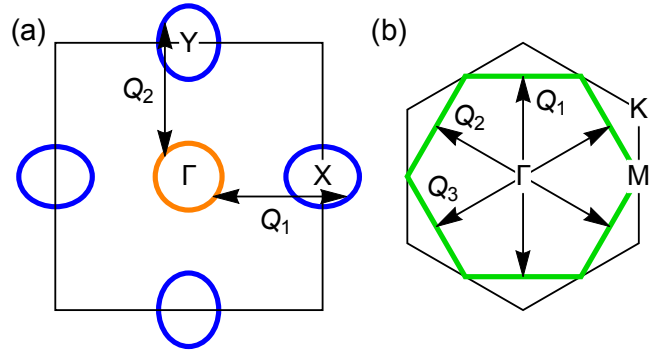


FIG. 1. **Schematic Fermi surfaces.** Illustration of electronic Fermi surfaces with characteristic nesting vectors with tetragonal (a) and triangular (b) underlying lattice structures.

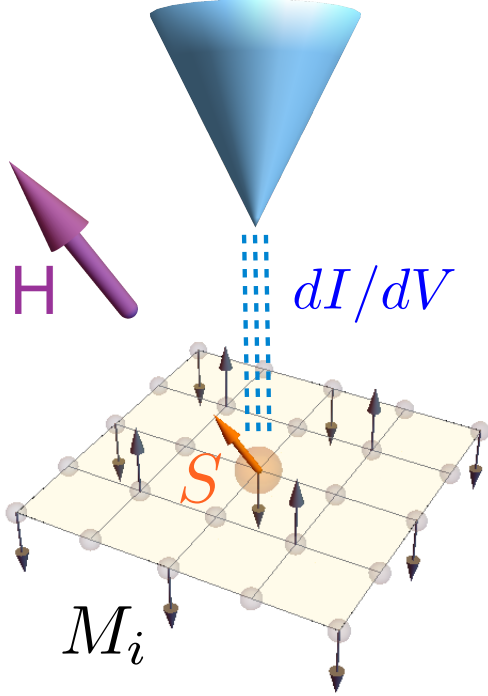


FIG. 2. **Illustration of proposed tunneling experiment.** The total tunneling conductance measured by an STM tip (blue tip) at the site of a magnetic impurity moment \mathbf{S} (orange arrow) embedded in a metallic host of itinerant electrons can be utilized to reveal the detailed magnetic structure of the host magnetism \mathbf{M}_i (black arrows). The external magnetic field \mathbf{H} is directed along the purple arrow and determines the direction of the impurity moment.

multi- \mathbf{Q} phases. Indeed, Mössbauer experiments have been recently employed to distinguish single- \mathbf{Q} versus double- \mathbf{Q} phases in iron-based superconductors¹⁸. In this paper, we propose theoretically that the magnetic field dependence of the LDOS, which can be obtained by performing STS measurements near a magnetic impurity, contains information that allows one to achieve this goal. In a nutshell, the local changes of the spin density amplitude induced around the impurity moment, are determined by the specific magnetic ground state of the host. They cause distinct LDOS signatures since the square of the local spin amplitude couples to the local charge density. We explain in detail this general framework and propose experimental realization for how to manipulate magnetic impurity moments interacting with the surrounding conduction electrons to pinpoint the nature of the magnetic ground state of itinerant systems. We illustrate the proposed setup in Fig. 2 and focus for concreteness on different proposed magnetic ground states relevant for iron-based superconductors.

Several theoretical calculations^{6,19–24} and experimental studies^{18,25–34} have revealed that these materials support not only a single- \mathbf{Q} magnetic stripe (MS) phase,

with ordering vectors $\mathbf{Q}_1 = (\pi, 0)$ or $\mathbf{Q}_2 = (0, \pi)$ [Fig. 4(c)], but also two possible types of double- \mathbf{Q} phases: a collinear double- \mathbf{Q} phase with non-uniform Fe-magnetization, called charge-spin density-wave (CSDW) [Fig. 4(a)], and a coplanar double- \mathbf{Q} phase called spin-vortex crystal (SVC)⁵ [Fig. 4(e)]. In the former, the staggered magnetization vectors corresponding to the two \mathbf{Q} vectors are parallel to each other, whereas in the latter they are perpendicular.

In the proposed STS experiment shown in Fig. 2, a small fraction of magnetic impurities such as Mn substitutes for Fe ions in a material which displays one of the possible magnetic configurations discussed above. On the one hand, the orientation of the itinerant ordered magnetic moments of the host system is fixed by the residual spin-orbit and magneto-elastic couplings. On the other hand, the coupling of the magnetic impurity to the host electronic system is determined by the Kondo-like interaction between the impurity and the conduction electrons J_K ^{35,36}, which in the case of Mn was found to be small by recent ESR studies³⁷. This property, allied to the insensitivity of the itinerant magnetism to external magnetic fields^{38,39}, implies that magnetic fields are able to “unlock” the magnetic moment of the impurity from the magnetic order in the lattice, thus allowing for a change of its orientation with respect to the rigid magnetic structure of the host system. In the simplest model in which the impurity moment orients itself parallel to the applied field, we calculate the impurity-modified LDOS structures as a function of external field direction for all three distinct magnetic ground states. We find qualitative differences in the obtained LDOS spectra and demonstrate that scanning tunneling spectroscopy offers a promising route to unambiguously distinguish single- \mathbf{Q} from multi- \mathbf{Q} magnetic phases.

MICROSCOPIC MODEL

We employ a Hamiltonian relevant to iron-pnictides, which consists of a five-orbital tight-binding term⁴⁰

$$\mathcal{H}_0 = \sum_{\mathbf{ij}, \mu\nu, \sigma} t_{\mathbf{ij}}^{\mu\nu} c_{\mathbf{i}\mu\sigma}^\dagger c_{\mathbf{j}\nu\sigma} - \mu_0 \sum_{\mathbf{i}\mu\sigma} n_{\mathbf{i}\mu\sigma}. \quad (1)$$

Interactions are included through the multi-orbital on-site Hubbard model

$$\begin{aligned} \mathcal{H}_{int} = & U \sum_{\mathbf{i}, \mu} n_{\mathbf{i}\mu\uparrow} n_{\mathbf{i}\mu\downarrow} + (U' - \frac{J}{2}) \sum_{\mathbf{i}, \mu < \nu, \sigma\sigma'} n_{\mathbf{i}\mu\sigma} n_{\mathbf{i}\nu\sigma'} \\ & - 2J \sum_{\mathbf{i}, \mu < \nu} \vec{S}_{\mathbf{i}\mu} \cdot \vec{S}_{\mathbf{i}\nu} + J' \sum_{\mathbf{i}, \mu < \nu, \sigma} c_{\mathbf{i}\mu\sigma}^\dagger c_{\mathbf{i}\mu\sigma}^\dagger c_{\mathbf{i}\nu\sigma} c_{\mathbf{i}\nu\sigma}, \end{aligned} \quad (2)$$

where μ, ν are orbital indices, \mathbf{i} denotes lattice sites, and σ is the spin. The interaction includes intraorbital (intraorbital) repulsion U (U'), the Hund’s coupling J , and the pair hopping term J' . Following previous studies²³

we assume spin and orbital rotation invariance, implying $U' = U - 2J$ and $J' = J$, and fix $J = U/4$. As shown previously in Ref. 23, the Hamiltonian $\mathcal{H} = \mathcal{H}_0 + \mathcal{H}_{int}$ supports all three magnetic ground states depending on interaction parameters and electron filling (details in the Supplementary Material (SM)). The resulting reconstructed Fermi surfaces in the magnetic phases are remarkably similar, and do not constitute a good probe of the preferred ordered phase (see also SM).

The magnetic impurity moment is included by the following term in the Hamiltonian

$$\mathcal{H}_S = \frac{J_K}{2} \sum_{\mu} \mathbf{S}_{\mathbf{i}^*} \cdot \left(c_{\mathbf{i}^* \mu \sigma}^{\dagger} \boldsymbol{\sigma}_{\sigma \sigma'} c_{\mathbf{i}^* \mu \sigma'} \right) - g \mu_B \mathbf{S}_{\mathbf{i}^*} \cdot \mathbf{H}. \quad (3)$$

The first term corresponds to the Kondo-like exchange coupling between the impurity moment $\mathbf{S}_{\mathbf{i}^*}$, located at site \mathbf{i}^* , and the spin of the itinerant electrons, which we denote hereafter by $\mathbf{M}_{\mathbf{i}}^0 \equiv \sum_{\mu} c_{\mathbf{i} \mu \sigma}^{\dagger} \boldsymbol{\sigma}_{\sigma \sigma'} c_{\mathbf{i} \mu \sigma'}$. The second term corresponds to the Zeeman coupling between the impurity moment and the external magnetic field \mathbf{H} . In principle, one would also need to include the Zeeman coupling between the itinerant moments and \mathbf{H} . However, as shown experimentally e.g. in Refs. 38 and 39, the itinerant magnetization is insensitive to magnetic fields of the order of 10 T, and therefore this term can be safely neglected. The main question is whether the external field \mathbf{H} is capable of rotating the impurity moment, which is also coupled to the itinerant electrons via J_K . To answer this question, we rely on ESR experiments that measured J_K for Mn-doped iron pnictides³⁷. The reported value $J_K \approx 0.8$ meV is very small, suggesting that magnetic fields of the order of 10 T (achievable in STM setups) can unlock the impurity moment from the itinerant magnetic configuration. Importantly, the fact that the Mn impurities act as local magnetic moments and do not add charge carriers into the system is supported by the NMR data in Refs. 27 and 36.

Therefore, we proceed by fixing the direction of $\mathbf{S}_{\mathbf{i}^*}$ to be parallel to \mathbf{H} , and introduce the polar angle θ between the magnetization of the itinerant electrons in the impurity-free system $\mathbf{M}_{\mathbf{i}^*}^0$ and the impurity moment $\mathbf{S}_{\mathbf{i}^*}$ at that site, $\cos \theta \propto \mathbf{S}_{\mathbf{i}^*} \cdot \mathbf{M}_{\mathbf{i}^*}^0$, as illustrated in Fig. 3(a). We use a magnetic impurity moment with $J_K S = 0.1$ meV, a value that is not important since our goal is to focus on the symmetry changes of the LDOS as the impurity moment rotates, i.e. as a function of the orientation θ . Thus, we solve Eqs. (1), (2), and (3) and calculate the LDOS $N(\mathbf{i}, \theta)$ at each lattice site according to

$$N(\mathbf{i}, \theta) = -\frac{1}{\pi} \text{Im} \sum_{n, \mu \sigma} \frac{u_{\mu \sigma}^n(\mathbf{i}, \theta) u_{\mu \sigma}^n(\mathbf{i}, \theta)}{\omega - E_n(\theta) + i\eta}. \quad (4)$$

Here $u_{\mu \sigma}^n(\mathbf{i}, \theta)$ are the matrix elements of the unitary transformation from orbital μ to eigenstate n . For further computational details, and spectral studies of the homogenous magnetic phases and the effects from non-magnetic disorder, we refer to the SM. The results are presented in Fig. 3 and discussed in details below.

RESULTS

The CSDW state. We start by discussing the results in the CSDW state. As illustrated in Figs. 3(a) and 3(b), in this collinear non-uniform double- \mathbf{Q} magnetic phase the even sites of the square lattice are non-magnetic, whereas the odd sites display a Neel-like magnetic configuration with spins parallel to the z direction. As a result, there are four inequivalent sites to place an impurity, two magnetic ($\mathbf{M}_{\mathbf{i}^*}^0 \neq 0$) and two non-magnetic ($\mathbf{M}_{\mathbf{i}^*}^0 = 0$) ones. Let us start discussing the modified magnetization around the impurity, which will be necessary to understand the resulting spectral signatures. The black arrows display the magnetization of the conduction electrons of the impurity-free system $\mathbf{M}_{\mathbf{i}}^0$, and the thick colored arrow indicates the impurity moment $\mathbf{S}_{\mathbf{i}^*}$. The induced spin density on the nearest neighbor (nn) sites $\mathbf{M}_{\mathbf{nn}}^{\text{ind}}$ is illustrated by the four arrows of the same color. The sum of the induced and impurity-free magnetizations yields the new total magnetization in the presence of the impurity, $\mathbf{M}_{\mathbf{i}} = \mathbf{M}_{\mathbf{i}}^0 + \mathbf{M}_{\mathbf{i}}^{\text{ind}}$. In our calculation, the induced spin density actually involves a larger number of sites surrounding the impurity moment, but for the symmetry arguments used below, it is sufficient to focus on the nn sites, where the effect is the largest.

We sketch in Fig. 3(e) the change in magnetic moment (projected along the $\hat{\mathbf{I}} = \hat{\mathbf{z}}$ axis) at the four nn sites induced by an impurity oriented along $\theta = 3\pi/4$, $(\Delta \mathbf{M}_{\mathbf{nn}})^2 \equiv (\mathbf{M}_{\mathbf{nn}} \cdot \hat{\mathbf{I}})^2 - (\mathbf{M}_{\mathbf{nn}}^0 \cdot \hat{\mathbf{I}})^2$. Clearly, the magnetization amplitude increases equally at all four nn sites, i.e. $|\mathbf{M}_{\mathbf{r}_1} \cdot \hat{\mathbf{I}}| = |\mathbf{M}_{\mathbf{r}_2} \cdot \hat{\mathbf{I}}|$, where $\mathbf{r}_1 = \mathbf{i}^* + \hat{\mathbf{x}}$ and $\mathbf{r}_2 = \mathbf{i}^* + \hat{\mathbf{y}}$ denote the two types of nn sites. If the same impurity moment is placed at a non-magnetic site, however, as illustrated in Fig. 3(b), the total projected moments on \mathbf{r}_1 and \mathbf{r}_2 become unequal. In particular, while the projected moment is reduced at the two sites along the y axis, it is enhanced at the sites along the x axis. This antagonistic change is sketched in Fig. 3(f). Consequently, the initial tetragonal symmetry of the magnetization is locally broken by the impurity, with $|\mathbf{M}_{\mathbf{r}_1} \cdot \hat{\mathbf{z}}| \neq |\mathbf{M}_{\mathbf{r}_2} \cdot \hat{\mathbf{z}}|$. For a general angle θ between the impurity moment and the itinerant magnetization, this symmetry breaking is given by the following expression,

$$|\mathbf{M}_{\mathbf{r}_1}|^2 - |\mathbf{M}_{\mathbf{r}_2}|^2 = (|\mathbf{M}_{\mathbf{r}_1}^{\text{ind}}|^2 - |\mathbf{M}_{\mathbf{r}_2}^{\text{ind}}|^2) - 2 (\mathbf{M}_{\mathbf{nn}}^0 \cdot \hat{\mathbf{z}}) (|\mathbf{M}_{\mathbf{r}_1}^{\text{ind}}| + |\mathbf{M}_{\mathbf{r}_2}^{\text{ind}}|) \cos \theta. \quad (5)$$

To make the argument more transparent, we assumed an anti-parallel orientation of $\mathbf{M}_{\mathbf{i}}^{\text{ind}}$ with respect to the impurity moment, which is strictly correct for an arbitrary θ only in the paramagnetic case, but it remains a reasonable approximation in our case. The full self-consistent result beyond this assumption is presented below.

To understand these results, we note that impurities at the magnetic sites of the CSDW phase [Fig. 3(a)] are subject to two constraints. First, the impurity-free SDW has nodes at the nn sites ($\mathbf{M}_{\mathbf{nn}}^0 \cdot \hat{\mathbf{z}} = 0$), and second, the symmetry of this site requires the induced moments

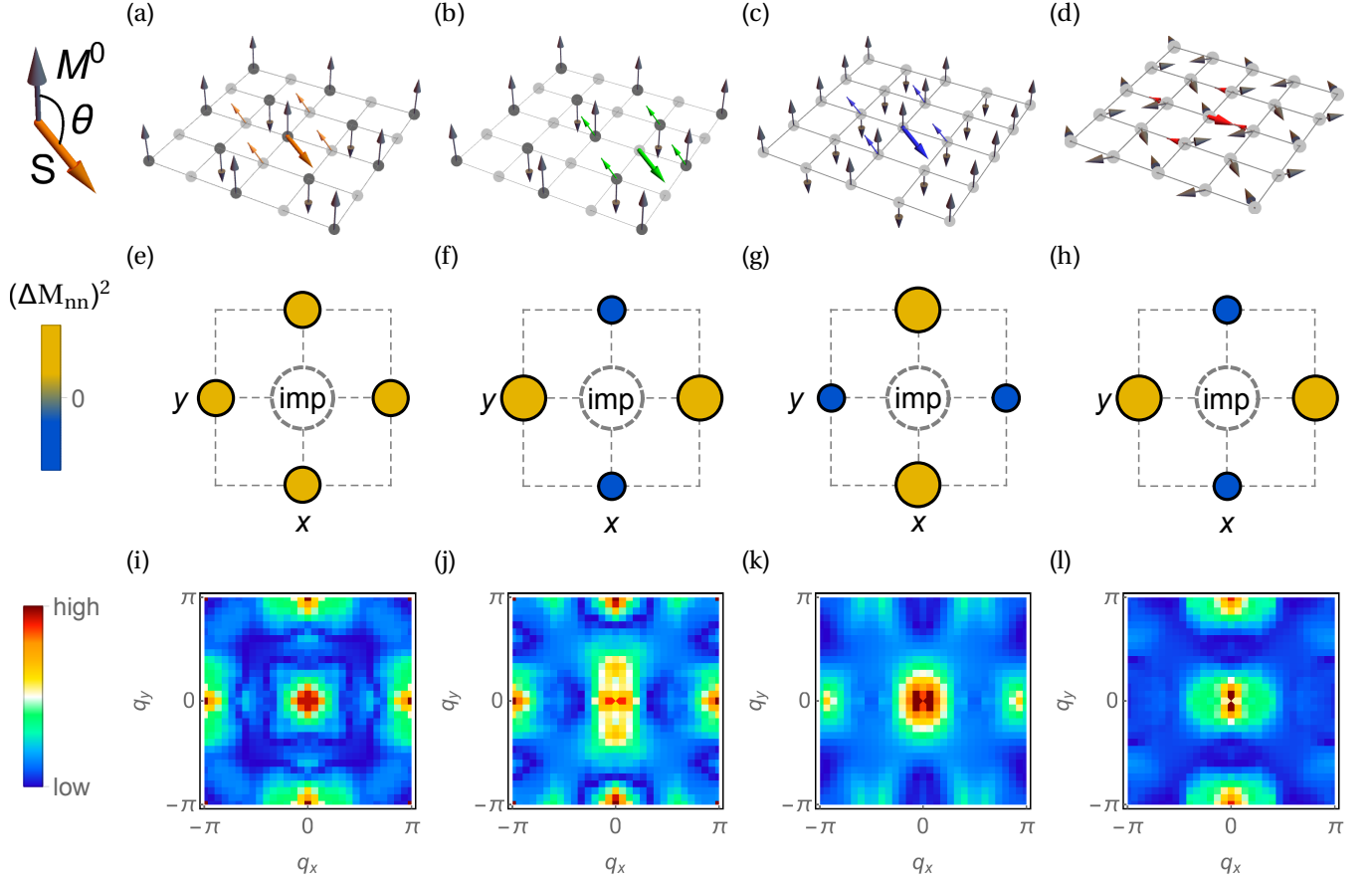


FIG. 3. **Connection between impurity-modified LDOS and the magnetic ground state.** Magnetic impurity (colored thick arrows) with $\theta = 3\pi/4$ orientation in the CSDW state (either in a magnetic site (a) or in a non-magnetic site (b)), in the MS state, and in the SVC state (d). The colored (black) arrows represent the induced (impurity-free) magnetization $\mathbf{M}_{\text{nn}}^{\text{ind}}$ at the nn sites (\mathbf{M}_i^0). (e)-(h) Sketches of the total moment amplitude deviation $(\Delta M)^2$ compared to the impurity-free case at the four nn sites ($(\Delta M_{\text{nn}})^2 \equiv [(\mathbf{M}_{\text{nn}} \cdot \hat{\mathbf{I}})^2 - (\mathbf{M}_{\text{nn}}^0 \cdot \hat{\mathbf{I}})^2] \hat{\mathbf{I}}$) in the previous four cases for (e)-(g) $\hat{\mathbf{I}} = \hat{\mathbf{z}}$ and (h) $\hat{\mathbf{I}} = \hat{\mathbf{x}}$ projection. Yellow (blue) denotes increased (decreased) amplitude. (i)-(l) The Fourier transformed LDOS $N(\mathbf{q}, \theta = 3\pi/4)$ of the (a)-(d) impurity configurations, respectively.

to be the same, $\mathbf{M}_{\mathbf{r}_1}^{\text{ind}} = \mathbf{M}_{\mathbf{r}_2}^{\text{ind}}$. Hence, $|\mathbf{M}_{\mathbf{r}_1}|^2 = |\mathbf{M}_{\mathbf{r}_2}|^2$ and tetragonal symmetry is preserved for any orientation of the impurity moment. By contrast, for impurity moments at non-magnetic sites, the difference between the total nn amplitudes has contributions from both terms in Eq. (5). Therefore, the symmetry-breaking expression is generally non-zero, and exhibits a cosine-like directional dependence.

Having established the basic effect of an impurity moment on the surrounding itinerant magnetic structure, we now study its consequences on the local spectral features. The total LDOS measures the spectral composition of the charge density, which is coupled by symmetry only to the magnetization density squared. Therefore, any change in the amplitude of the spin density will have an impact on the LDOS. For instance, a C_4 (C_2) symmetric magnetic structure will generally present C_4 (C_2) symmetric LDOS signatures (here C_4 and C_2 denote tetragonal and orthorhombic symmetries). Fig. 3(i) shows the Fourier transformed LDOS of the case displayed in Fig. 3(a),

$N(\mathbf{q}, 3\pi/4)$. Clearly, the C_4 symmetry of the pristine CSDW state is preserved around the impurity, in agreement with the magnetic moment structure sketched in Fig. 3(e) and the result $|\mathbf{M}_{\mathbf{r}_1}|^2 = |\mathbf{M}_{\mathbf{r}_2}|^2$ given by Eq. (5). The spectral symmetry is in fact tetragonal for all possible orientations of the impurity in the CSDW phase, as long as the impurity moment is placed at a magnetic site. If the same impurity moment is placed at a non-magnetic site, however, as illustrated in Fig. 3(b), $N(\mathbf{q}, 3\pi/4)$ becomes C_2 symmetric as seen in Fig. 3(j). This is simply a consequence of the C_2 symmetric spin structure induced by the impurity discussed earlier and sketched in Fig. 3(f).

In order to quantify the evolution of the spectral symmetry of the LDOS as the impurity rotates, and compare it to Eq. (5), we introduce the anisotropy parameter

$$\delta_{C_2}(\theta) = \sum_{\mathbf{i}} \frac{|N(\mathbf{i}, \theta) - N(R\{\mathbf{i}\}, \theta)|}{N(\mathbf{i}, \theta) + N(R\{\mathbf{i}\}, \theta)}, \quad (6)$$

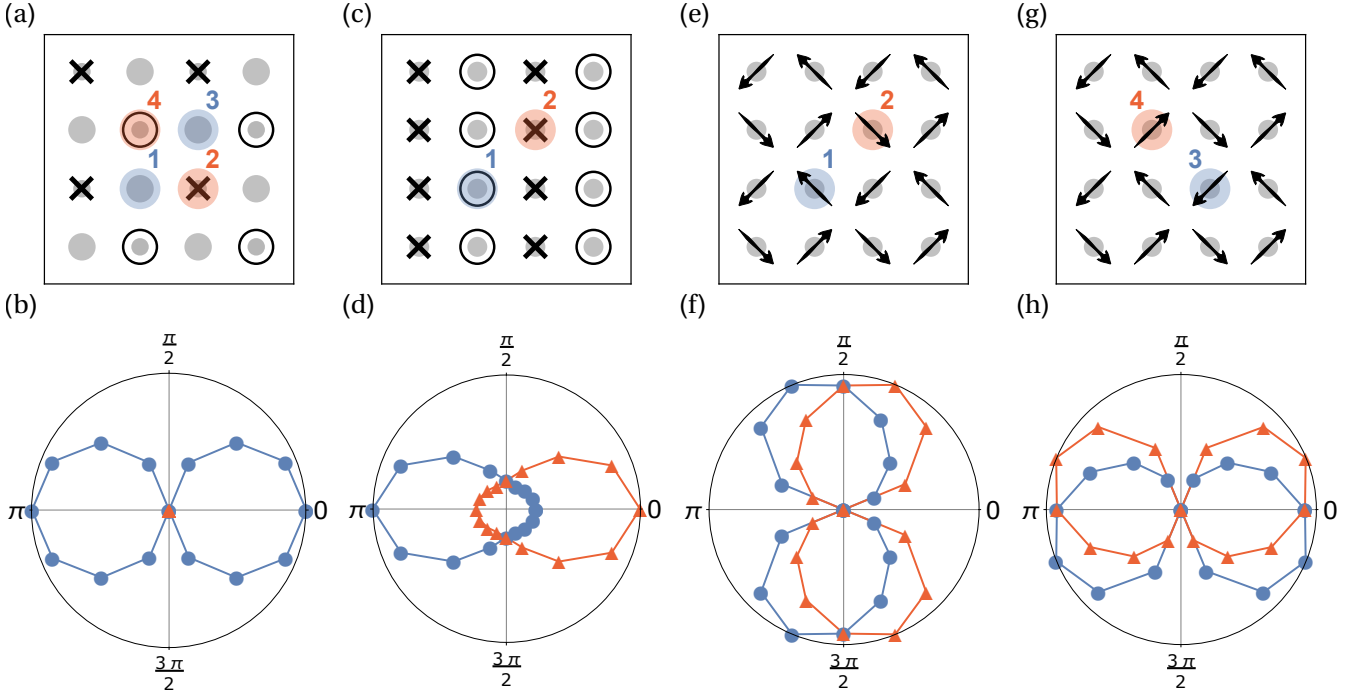


FIG. 4. **Angular dependence of C_4 -symmetry breaking in the LDOS.** Spectral symmetry breaking parameter $\delta_{C_2}(\theta)$ [see Eq. (6)] as a function of the orientation of the magnetic impurity θ in the inequivalent sites of the magnetic states. θ represents the polar angle in the (a)-(b) CSDW and (c)-(d) MS states, and (e)-(h) the azimuthal angle in the SVC state. $\theta = 3\pi/4$ examples are explicitly shown in Fig. 3. (b),(d), (f) and (h) are polar plots of the average $\delta_{C_2}(\theta)$ as radius in a given direction θ in the xz (xy) plane for all relevant inequivalent sites of the CSDW and MS (CSV) states.

which measures the breaking of the C_4 symmetry for a given θ . Here R denotes a $\pi/2$ rotation operation. Figure 4(b) shows the evolution of δ_{C_2} as a function of θ from the calculated LDOS at all four inequivalent sites in the CSDW state, specified in Fig. 4(a). As seen, tetragonal symmetry is indeed preserved for all θ at the magnetic sites (2 and 4), but broken in a cosine-like fashion at the non-magnetic sites (1 and 3), in agreement with the above discussion.

The MS state. The single- \mathbf{Q} MS phase corresponds to the case in which only one of the two possible \mathbf{Q} vectors is selected. The corresponding magnetic configuration, shown in Fig. 3(c), breaks the C_4 symmetry down to C_2 , in contrast to the double- \mathbf{Q} magnetic configurations, which preserve tetragonal symmetry. We now consider the effects of an impurity moment with $\theta = 3\pi/4$ orientation with respect to the SDW magnetization. The inequivalent change in the spin projection along the z axis of the four nn sites is illustrated in Fig. 3(g), which accounts for the symmetry breaking in the corresponding $N(\mathbf{q}, 3\pi/4)$ shown in Fig. 3(k). The evolution of $\delta_{C_2}(\theta)$ for the two inequivalent sites in this state can be seen in Fig. 4(d). Clearly, both sites (specified in Fig. 4(c)) give rise to distinct angular evolutions which break C_2 symmetry. This is in contrast to what was found in the CSDW state, where half of the sites exhibit a C_2 -symmetric cosine-like evolution of $\delta_{C_2}(\theta)$, and the other half preserve C_4 symmetry for all impurity orientations,

$\delta_{C_2}(\theta) = 0$.

The SVC state. Finally we discuss the case of a magnetic impurity in the coplanar SVC phase. In this double- \mathbf{Q} magnetic state, the even sites of the square lattice display a Neel-like order that is perpendicular to the Neel-like order displayed by the odd sites. As a result, there are four inequivalent sites. One of them is shown in Fig. 3(d), with the calculated LDOS displayed in Fig. 3(l). Again, the C_2 symmetric spectral features can be connected to the different moment amplitudes at the nn sites, as illustrated in Fig. 3(h) for projections along the x axis. The angular evolution of $\delta_{C_2}(\theta)$ in the four inequivalent sites (in the xy plane for this state) is shown in Fig. 4(f,h). Contrary to what was found in the CSDW phase, all inequivalent sites show a $\delta_{C_2}(\theta)$ spectral angular dependence with broken C_2 symmetry. Moreover, the angular dependences appear identical but shifted by $n\pi/2$ for all four inequivalent sites ($n = 1, 2, 3$), which is a consequence of the uniform moment amplitude $|\mathbf{M}_i^0| = M^0$ in the SVC state.

DISCUSSION

The results presented in the previous section open different routes to distinguish between single- \mathbf{Q} and multi- \mathbf{Q} magnetic ground states via STS experiments. The most direct way would be to extract the LDOS anisotropy

parameter δ_{C_2} as function of the angle θ between the applied magnetic field and the magnetization. Note that a recent STS experiment on the iron pnictide NaFeAs extracted precisely this anisotropy parameter (for zero magnetic field)⁴¹. As shown in Fig. 4, the function $\delta_{C_2}(\theta)$ behaves qualitatively different for each of the three magnetic ground states:

- In the CSDW state, experiments would only observe a single anisotropy parameter curve $\delta_{C_2}(\theta)$, which displays a cosine-like C_2 symmetric shape [Fig. 4(b)]. This curve corresponds to a magnetic impurity placed in a magnetic site, since impurities located at non-magnetic sites exhibit fully C_4 -symmetric LDOS.
- In the MS state, experiments would observe two anisotropy parameter curves $\delta_{C_2}(\theta)$ [Fig. 4(d)]. These two curves, related to the two inequivalent site positions in the magnetic ground state, are simply related by a $\theta = \pi$ shift. In addition, tetragonal symmetry is broken for *all* impurity orientations, i.e. $\delta_{C_2}(\theta) \neq 0$ for all θ values.
- In the SVC state, experiments would observe four anisotropy parameter curves $\delta_{C_2}(\theta)$ [Fig. 4(f,h)]. They also correspond to the four inequivalent site positions of the SVC state, and are related to each other by successive shifts of $\theta = \pi/2$.

While a continuous rotation of the magnetic field may be experimentally challenging, our results can also be useful in cases where the direction of the field can only

be changed from “positive” to “negative.” Assume, for example, that only the angles $\theta = 0$ and $\theta = \pi$ are experimentally accessible. Then, as can be inferred from panels (b), (d) and (f) in Fig. 4, one may still use the measured LDOS to deduce the true ground state. Alternatively, the Fourier transformation of the LDOS for two fixed angles, can also be used to constrain the possible ground states – see panels (i)-(l) in Fig. 3.

The proposed experiment advocated in this paper relies on the fact that an impurity moment can be controlled by an external applied field which, however, does not significantly affect the itinerant magnetic order. In addition, it would be desirable if this impurity did not introduce additional charge carriers in the system. In the case of the iron-pnictides, Mn impurities are natural candidates, since they form local moments weakly coupled to the itinerant system^{27,36,37}, which is itself robust against moderate magnetic fields³⁸. It will be interesting to extend our calculations to multi- \mathbf{Q} magnetic phases in triangular lattices, where exotic triple- \mathbf{Q} phases can appear. Our work provides a promising avenue for future tunneling spectroscopy to directly distinguish between nearly degenerate but symmetry-distinct magnetic ground states of itinerant magnetic systems.

ACKNOWLEDGMENTS

M.N.G. and B.M.A. acknowledge support from Lundbeckfond fellowship (grant A9318). R.M.F is supported by the Office of Basic Energy Sciences, U.S. Department of Energy, under award de-sc0012336.

¹ O. A. Starykh, Rep. Prog. Phys. **78**, 052502 (2015).
² L. Balents, Nature **464**, 199 (2010).
³ S. Hayami and Y. Motome, Phys. Rev. B **90**, 060402(R) (2014).
⁴ J. W. F. Venderbos, Phys. Rev. B **93**, 115108 (2016).
⁵ R. M. Fernandes, S. A. Kivelson, and E. Berg, Phys. Rev. B **93**, 014511 (2016).
⁶ I. Eremin and A. V. Chubukov, Phys. Rev. B **81**, 024511 (2010).
⁷ R. M. Fernandes, A. V. Chubukov, and J. Schmalian, Nature Phys. **10**, 97 (2014).
⁸ B. Roy, J. Hofmann, V. Stanev, J. D. Sau, and V. Galitski, Phys. Rev. B **92**, 245431 (2015).
⁹ I. Martin and C. D. Batista, Phys. Rev. Lett. **101**, 156402 (2008).
¹⁰ M. Kiesel, C. Platt, W. Hanke, D. A. Abanin, and R. Thomale, Phys. Rev. B **86**, 020507 (2012).
¹¹ W.-S. Wang, Y.-Y. Xiang, Q.-H. Wang, F. Wang, F. Yang, and D.-H. Lee, Phys. Rev. B **85**, 035414 (2012).
¹² R. Nandkishore, G.-W. Chern, and A. V. Chubukov, Phys. Rev. Lett. **108**, 227204 (2012).
¹³ D. Mendler, P. Kotetes, G. Schön, Phys. Rev. B **91**, 155405 (2015).
¹⁴ B. Barbara, M. F. Rossignol, J. X. Boucherle, and C. Vettier, Phys. Rev. Lett. **45**, 938 (1980).

¹⁵ J. Jensen and P. Bak, Phys. Rev. B **23**, 6180(R) (1981).
¹⁶ J. Jensen and M. Rotter, Phys. Rev. B **77**, 134408 (2008).
¹⁷ R. S. Fishman and S. H. Liu, Phys. Rev. B **59**, 8681 (1999).
¹⁸ J. M. Allred, K. M. Taddei, D. E. Bugaris, M. J. Krogstad, S. H. Lapidus, D. Y. Chung, H. Claus, M. G. Kanatzidis, D. E. Brown, J. Kang, R. M. Fernandes, I. Eremin, S. Rosenkranz, O. Chmaissem, and R. Osborn, Nature Phys. **00** (2016).
¹⁹ J. Lorenzana, G. Seibold, C. Ortiz, and M. Grilli, Phys. Rev. Lett. **101**, 186402 (2008).
²⁰ G. Giovannetti, C. Ortix, M. Marsman, M. Capone, J. van den Brink, and J. Lorenzana, Nat. Commun. **2**, 398 (2011).
²¹ M. N. Gastiasoro and B. M. Andersen, Phys. Rev. Lett. **113**, 067002 (2014).
²² J. Kang, X. Wang, A. V. Chubukov, and R. M. Fernandes, Phys. Rev. B **91**, 121104(R) (2015).
²³ M. N. Gastiasoro and B. M. Andersen, Phys. Rev. B **92**, 150506(R) (2015).
²⁴ M. H. Christensen, J. Kang, B. M. Andersen, I. Eremin, R. Fernandes, Phys. Rev. B **92**, 214509 (2015).
²⁵ M. G. Kim, A. Kreyssig, A. Thaler, D. K. Pratt, W. Tian, J. L. Zarestky, M. A. Green, S. L. Budko, P. C. Canfield, R. J. McQueeney, and A. I. Goldman, Phys. Rev. B **82**, 220503(R) (2010).

- ²⁶ S. Avci, O. Chmaissem, S. Rosenkranz, J. M. Allred, I. Eremin, A. V. Chubukov, D. Y. Chung, M. G. Kanatzidis, J.-P. Castellan, J. A. Schlueter, H. Claus, D. D. Khalyavin, P. Manuel, A. Daoud-Aladine, and R. Osborn, *Nat. Commun.* **5**, 3845 (2014).
- ²⁷ D. S. Inosov, G. Friemel, J. T. Park, A. C. Walters, Y. Texier, Y. Laplace, J. Bobroff, V. Hinkov, D. L. Sun, Y. Liu, R. Khasanov, K. Sedlak, Ph. Bourges, Y. Sidis, A. Ivanov, C. T. Lin, T. Keller, and B. Keimer, *Phys. Rev. B* **87**, 224425 (2013).
- ²⁸ E. Hassinger, G. Gredat, F. Valade, S. René de Cotret, A. Juneau-Fecteau, J.-Ph. Reid, H. Kim, M. A. Tanatar, R. Prozorov, B. Shen, H.-H. Wen, N. Doiron-Leyraud, and L. Taillefer, *Phys. Rev. B* **86**, 140502(R) (2012).
- ²⁹ F. Waßer, A. Schneidewind, Y. Sidis, S. Wurmehl, S. Aswartham, B. Büchner, and M. Braden, *Phys. Rev. B* **91**, 060505(R) (2015).
- ³⁰ A. E. Böhrer, F. Hardy, L. Wang, T. Wolf, P. Schweiss, and C. Meingast, *Nat. Commun.* **6**, 7911 (2015).
- ³¹ B. P. P. Mallett, P. Marsik, M. Yazdi-Rizi, T. Wolf, A. Böhrer, F. Hardy, C. Meingast, D. Munzar, and C. Bernhard, *Phys. Rev. Lett.* **115**, 027003 (2015).
- ³² J. M. Allred, S. Avci, D. Y. Chung, H. Claus, D. D. Khalyavin, P. Manuel, K. M. Taddei, M. G. Kanatzidis, S. Rosenkranz, R. Osborn, and O. Chmaissem, *Phys. Rev. B* **92**, 094515 (2015).
- ³³ B. P. P. Mallett, Yu. G. Pashkevich, A. Gusev, Th. Wolf, C. Bernhard, *Europhys. Lett.* **111**, 57001 (2015).
- ³⁴ E. Hassinger, G. Gredat, F. Valade, S. René de Cotret, O. Cyr-Choiniere, A. Juneau-Fecteau, J.-Ph. Reid, H. Kim, M. A. Tanatar, R. Prozorov, B. Shen, H.-H. Wen, N. Doiron-Leyraud, Louis Taillefer, arXiv:1512.05912v1.
- ³⁵ Y. Texier, Y. Laplace, P. Mendels, J. T. Park, G. Friemel, D. L. Sun, D. S. Inosov, C. T. Lin, and J. Bobroff, *Europhys. Lett.* **99**, 17002 (2012).
- ³⁶ D. LeBoeuf, Y. Texier, M. Boselli, A. Forget, D. Colson, and J. Bobroff, *Phys. Rev. B* **89**, 035114 (2014).
- ³⁷ P. F. S. Rosa, C. Adriano, T. M. Garitezi, M. M. Piva, K. Mydeen, T. Grant, Z. Fisk, M. Nicklas, R. R. Urbano, R. M. Fernandes, and P. G. Pagliuso, *Sci. Rep.* **4**, 6252 (2014).
- ³⁸ M. Wang, H. Luo, M. Wang, S. Chi, J. A. Rodriguez-Rivera, D. Singh, S. Chang, J. W. Lynn, and P. Dai, *Phys. Rev. B* **83**, 094516 (2011).
- ³⁹ M. Enayat, Z. Sun, U. R. Singh, R. Aluru, S. Schmaus, A. Yaresko, Y. Liu, C. Lin, V. Tsurkan, A. Loidl, J. Deisenhofer, and P. Wahl, *Science* **345**, 6197 (2014).
- ⁴⁰ H. Ikeda, R. Arita, and J. Kunes, *Phys. Rev. B* **81**, 054502 (2010).
- ⁴¹ E. P. Rosenthal, E. F. Andrade, C. J. Arguello, R. M. Fernandes, L. Y. Xing, X. C. Wang, C. Q. Jin, A. J. Millis, and A. N. Pasupathy, *Nature Phys.* **10**, 225 (2014).

Supplemental Materials: "Scanning tunneling spectroscopy as a probe of multi-Q magnetic states of itinerant magnets"

Here, we provide computational details and a band structure description of the paramagnetic and magnetic states. We also include a brief spectroscopic study of non-magnetic impurities in the three magnetic states, where we discuss both spin-summed and spin-resolved features.

I. COMPUTATIONAL DETAILS

A mean field decoupling in the spin and charge channels leads to the following total Hamiltonian

$$\mathcal{H}^{MF} = \sum_{\mathbf{i}j\mu\nu} \begin{pmatrix} \hat{c}_{\mathbf{i}\mu\uparrow}^\dagger & \hat{c}_{\mathbf{i}\mu\downarrow}^\dagger \end{pmatrix} \begin{pmatrix} \varphi_{\mathbf{ij}}^{\mu\nu} & \omega_{\mathbf{ii}}^{\mu\nu} \\ \omega_{\mathbf{ij}}^{\mu\nu} & \varphi_{\mathbf{ij}}^{\mu\nu} \end{pmatrix} \begin{pmatrix} \hat{c}_{\mathbf{j}\nu\uparrow} \\ \hat{c}_{\mathbf{j}\nu\downarrow} \end{pmatrix}, \quad (\text{S1})$$

where $\hat{c}_{\mathbf{i}\mu\sigma}^\dagger$ creates an electron at site \mathbf{i} with spin σ in orbital state μ . $\varphi_{\mathbf{ij}}^{\mu\nu}$ and $\omega_{\mathbf{ii}}^{\mu\nu}$ are given by

$$\varphi_{\mathbf{ij}}^{\mu\nu} = t_{\mathbf{ij}}^{\mu\nu} + \delta_{\mu\nu} [-\mu_0 + (\Omega_\mu^0 + \Omega_\mu^z) \delta_{\mathbf{ii}^*} \delta_{\mu\nu} + U \langle \hat{n}_{\mathbf{i}\mu\bar{\sigma}} \rangle + U' \langle \hat{n}_{\mathbf{i}\nu\bar{\sigma}} \rangle + (U' - J) \langle \hat{n}_{\mathbf{i}\nu\sigma} \rangle] \quad (\text{S2})$$

$$\begin{aligned} & - \bar{\delta}_{\mu\nu} [(U' - J) \langle \hat{c}_{\mathbf{i}\nu\sigma}^\dagger \hat{c}_{\mathbf{i}\mu\sigma} \rangle + J \langle \hat{c}_{\mathbf{i}\nu\bar{\sigma}}^\dagger \hat{c}_{\mathbf{i}\mu\bar{\sigma}} \rangle + J' \langle \hat{c}_{\mathbf{i}\mu\bar{\sigma}}^\dagger \hat{c}_{\mathbf{i}\nu\bar{\sigma}} \rangle], \\ \omega_{\mathbf{ii}}^{\mu\nu} &= \delta_{\mu\nu} [\Omega_\mu^x \delta_{\mathbf{ii}^*} \delta_{\mu\nu} - U \langle \hat{c}_{\mathbf{i}\mu\bar{\sigma}}^\dagger \hat{c}_{\mathbf{i}\mu\sigma} \rangle - J \langle \hat{c}_{\mathbf{i}\nu\bar{\sigma}}^\dagger \hat{c}_{\mathbf{i}\nu\sigma} \rangle] - \bar{\delta}_{\mu\nu} [U' \langle \hat{c}_{\mathbf{i}\nu\bar{\sigma}}^\dagger \hat{c}_{\mathbf{i}\mu\sigma} \rangle + J' \langle \hat{c}_{\mathbf{i}\mu\bar{\sigma}}^\dagger \hat{c}_{\mathbf{i}\nu\sigma} \rangle], \end{aligned} \quad (\text{S3})$$

with $\bar{\delta}_{\mu\nu} = 1 - \delta_{\mu\nu}$. The terms $\Omega_\mu^z = \sigma J_K \mathbf{S}_\mu \cdot \hat{z}$ and $\Omega_\mu^x = J_K \mathbf{S}_\mu \cdot \hat{x}$ include out-of-plane and in-plane components of a magnetic impurity at site \mathbf{i}^* , respectively. A non-magnetic scatterer can be also introduced at the same site by the $\Omega_\mu^0 = V_\mu$ term. In the main text this last term was set to zero, but for a brief non-magnetic impurity study the reader is referred to the next section. We diagonalize Eq.(S1) on 30×30 lattices by a unitary transformation $\hat{c}_{\mathbf{i}\mu\sigma} = \sum_n u_{\mu\sigma}^n(\mathbf{i}) \hat{\gamma}_n$, and the following unrestricted fields are obtained self-consistently

$$\begin{aligned} \langle \hat{c}_{\mathbf{i}\mu\sigma}^\dagger \hat{c}_{\mathbf{j}\nu\sigma} \rangle &= \sum_n u_{\mu\sigma}^{n*}(\mathbf{i}) u_{\nu\sigma}^n(\mathbf{j}) f(E_n), \\ \langle \hat{c}_{\mathbf{i}\mu\sigma}^\dagger \hat{c}_{\mathbf{i}\nu\bar{\sigma}} \rangle &= \sum_n u_{\mu\sigma}^{n*}(\mathbf{i}) u_{\nu\bar{\sigma}}^n(\mathbf{i}) f(E_n), \end{aligned} \quad (\text{S4})$$

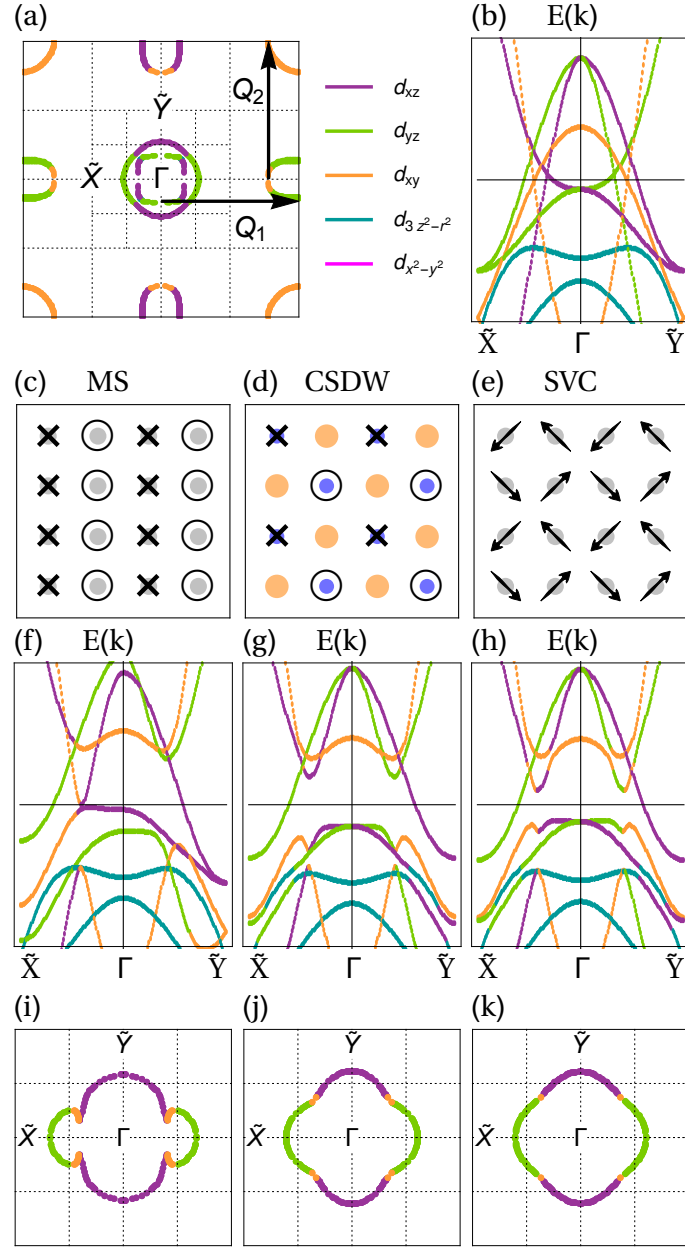


FIG. S1. (a) Fermi surface of the normal state and (b) its band dispersion $E(k)$ along high symmetry lines in the folded BZ (FBZ) obtained by folding the original BZ by \mathbf{Q}_1 and \mathbf{Q}_2 . The colors represent the main orbital content, specified in the legend. (c-e) The three SDW states MS (c), CSDW (d) with out-of-plane oriented moments and (π, π) charge order with orange (blue) indicating high (low) electron density n , and SVC (e). The band dispersions (f)-(h) and Fermi surfaces in the FBZ (i)-(k) for the three respective SDW phases in (c-e).

for all sites \mathbf{i}, \mathbf{j} and orbital combinations μ, ν . Here E_n denote the eigenvalues, and f is the Fermi function. The magnetization density $\mathbf{M}_i = \sum_{\mu\sigma\sigma'} \langle \hat{c}_{i\mu\sigma}^\dagger \boldsymbol{\sigma}_{\sigma\sigma'} \hat{c}_{i\mu\sigma'} \rangle$ ($\mu_B = 1$, $g = 2$) and charge density $n_i = \sum_{\mu\sigma} \langle \hat{c}_{i\mu\sigma}^\dagger \hat{c}_{i\mu\sigma} \rangle$ are obtained from the self-consistent fields in Eq. (S4).

II. HOMOGENEOUS BAND STRUCTURE

For the band structure relevant to the iron pnictides, three hole-like and two electron-like bands cross the Fermi level, with two degenerate nesting vectors $\mathbf{Q}_1 = (\pi, 0)$ and $\mathbf{Q}_2 = (0, \pi)$, as shown in Fig. S1(a,b). The corresponding RPA spin susceptibility is peaked at \mathbf{Q}_1 and \mathbf{Q}_2 , and in general the spin ordered state will be a combination of both ordering vectors, $\mathbf{M}(\mathbf{r}) = \sum_{l=1,2} \mathbf{M}_l \exp(i\mathbf{Q}_l \cdot \mathbf{r})$.^{S1-S3} The spin structures of the three distinct magnetic states are shown in Figs. S1(c)-(e). For these systems, the prevalent magnetic phase is the MS state with in-plane moments along the antiferromagnetic ordering vector. Interestingly, the new experimentally observed magnetic phase exhibits a spin reorientation from in-plane to out-of-plane, with moments along the c axis.^{S4} The relevant spin structures for this new phase are thus collinear single- \mathbf{Q} MS and double- \mathbf{Q} CSDW states with out-of-plane moments, which we consider in this work (Figs. S1(c)-(d)).

In order to compare the resulting electronic properties of the three SDW states at an equal footing, we fix the temperature to $\kappa_B T = 10$ meV, the electron filling $n = 5.88$, and the interaction parameters $U = 0.95$ eV. In this region of parameter space, the CSDW state is the global minimum.^{S5} The other two magnetic states are local minima, which may be stabilized self-consistently by applying restrictions to the fields. In this way all three magnetic states are generated from the same normal state [Figs. S1(a)-(b)]. Figures S1(f)-(k) show the reconstructed Fermi surfaces and band structures of the three different SDW states along high symmetry lines in the folded Brillouin zone (FBZ) ($-\pi/2 < k_x, k_y < \pi/2$). In the single- \mathbf{Q} MS state only SDW gaps at momenta connected by the ordering vector \mathbf{Q}_1 open, leaving the direction parallel to the stripes metallic, and thus resulting in a C_2 symmetric band dispersion and Fermi surface shown in Figs. S1(f) and S1(i), respectively. In the double- \mathbf{Q} states, the gaps open at momenta connected by both \mathbf{Q}_1 and \mathbf{Q}_2 , resulting in two very similar band reconstructions with almost identical Fermi surfaces, as seen by comparison of Figs. S1(g)-(h) and Figs. S1(j)-(k), despite their very different magnetic structures in real space.

III. NONMAGNETIC IMPURITY

In this section we briefly analyze the effects of a non-magnetic impurity introduced by the term

$$\mathcal{H}_p = V_p \sum_{\mu\sigma} c_{\mathbf{i}^* \mu\sigma}^\dagger c_{\mathbf{i} \mu\sigma}, \quad (\text{S5})$$

which adds a local spin-less potential at site \mathbf{i}^* . The orbitally diagonal potential V_p is a good approximation in these systems^{S6}. We calculate the projected spin resolved LDOS

$$N_{\sigma\sigma'}(\mathbf{i}) = -\frac{1}{\pi} \text{Im}(\mathcal{G}_{\sigma\sigma'}(\mathbf{i}, \omega)) = -\frac{1}{\pi} \text{Im} \sum_{n,\mu} \frac{u_{\mathbf{i}\mu\sigma}^n u_{\mathbf{i}\mu\sigma'}^n}{\omega - E_n + i\eta}, \quad (\text{S6})$$

to get the total LDOS $N(\mathbf{i}) = \sum_{\sigma\sigma'} N_{\sigma\sigma'}(\mathbf{i})$, and the local spin-polarization of the electrons at the Fermi energy ($\omega = 0$), $\mathbf{P}(\mathbf{i}) = \text{Tr}(\boldsymbol{\sigma}_{\sigma\sigma'} N_{\sigma\sigma'}(\mathbf{i})) / N(\mathbf{i})$.

Figures S2(a)-(c) display the resulting LDOS at $\omega = 0$ around a $V_p = 0.5$ eV potential placed in each of the three different magnetic states. In the MS state [Fig. S2(a)] the impurity reflects the broken C_4 symmetry of the homogeneous system. By contrast, the tetragonal symmetry is preserved around the potential in both double- \mathbf{Q} phases as seen from Figs. S2(b) and S2(c). In the CSDW case there is a (π, π) modulation in $N(\mathbf{i})$, arising from the charge order at $\mathbf{q} = \mathbf{Q}_1 + \mathbf{Q}_2$ of the homogeneous state. The (π, π) charge modulation constitutes a strong STM fingerprint of the CSDW ordered state. The amplitude of this modulation, however, may be too small to be easily detected by tunneling spectroscopy. This implies that there is no simple way to distinguish the SVC and CSDW phases by use of a non-magnetic potential scatterer.

The local spin polarization $\mathbf{P}(\mathbf{i})$ gives complementary information that would, in principle, allow one to distinguish between the CSDW and the SVC phases from the spin-polarized tunneling conductance. We show in Figs. S2(d)-(f) the polarization at the Fermi level for the relevant spin projection $\hat{\mathbf{l}}$ of the three magnetic states ($\mathbf{P}(\mathbf{i}) \cdot \hat{\mathbf{l}} \propto \mathbf{M}_i \cdot \hat{\mathbf{l}}$). This property is related to the magnetic contrast measured in a spin-polarized STM experiment^{S7}. The polarization of the single- \mathbf{Q} state in Fig. S2(d) consists of \mathbf{Q}_1 modulated stripes for the $\hat{\mathbf{l}} = \hat{\mathbf{z}}$ projection. The $\hat{\mathbf{l}} = \hat{\mathbf{x}}$ and $\hat{\mathbf{l}} = \hat{\mathbf{y}}$ components have no polarization, since $\mathbf{M}_i \cdot \hat{\mathbf{l}} = 0$ in the xy plane [Fig. S1(c)]. In the case of the CSDW state, the relevant projection is also the $\hat{\mathbf{z}}$ axis [Fig. S1(d)], where half of the sites appear with alternating polarization and the other half are not polarized, resulting from an equal superposition of \mathbf{Q}_1 and \mathbf{Q}_2 parallel spin density waves. Note that the C_4 symmetry is preserved in the polarization pattern around the impurity in this state. The last magnetic

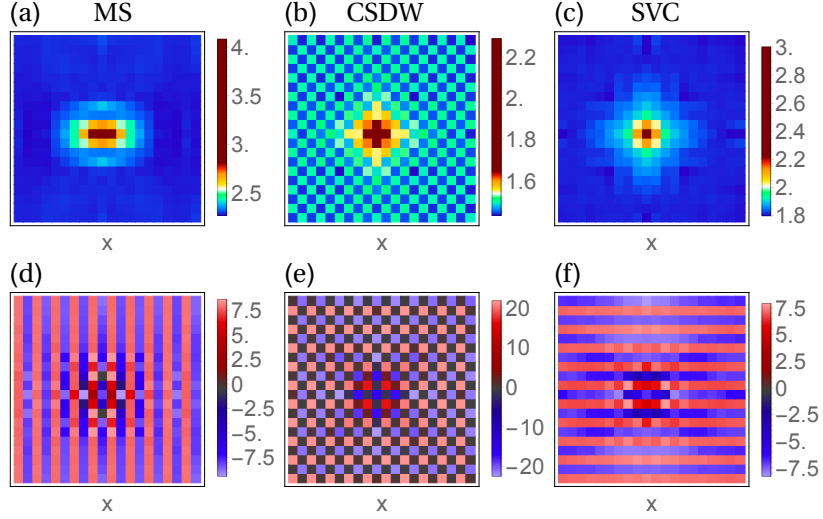


FIG. S2. (a,c) Total (spin-summed) LDOS $N(\mathbf{i})$ at $\omega = 0$ around a $V_p = 0.5$ eV non-magnetic impurity in the (a) MS, (b) CSDW, and (c) SVC states. (d-f) Local spin polarization percent $\mathbf{P}(\mathbf{i}) \cdot \hat{\mathbf{I}}$ [%] of the corresponding cases in the upper row with $\hat{\mathbf{I}} = \hat{\mathbf{z}}, \hat{\mathbf{z}}$ and $\hat{\mathbf{x}}, \hat{\mathbf{x}}$, respectively.

state, the SVC, with a coplanar spin structure [Fig. S1(e)] has two relevant spin projections, the in-plane $\hat{\mathbf{I}} = \hat{\mathbf{x}}$ and $\hat{\mathbf{I}} = \hat{\mathbf{y}}$. \mathbf{Q}_2 modulated stripes can be seen in Fig. S2(f) for $\hat{\mathbf{I}} = \hat{\mathbf{x}}$, with a local C_2 symmetric polarization pattern around the impurity. The perpendicular $\hat{\mathbf{I}} = \hat{\mathbf{y}}$ polarization (not shown) consists of \mathbf{Q}_1 stripes, similar to those in the MS state [Fig. S2(d)]. The two double- \mathbf{Q} phases are now clearly discernible, with distinctive local and global spin-polarization tunneling.

-
- [S1] I. Eremin and A. V. Chubukov, Phys. Rev. B **81**, 024511 (2010).
 - [S2] J. Lorenzana, G. Seibold, C. Ortiz, and M. Grilli, Phys. Rev. Lett. **101**, 186402 (2008).
 - [S3] G. Giovannetti, C. Ortix, M. Marsman, M. Capone, J. van den Brink, and J. Lorenzana, Nat. Commun. **2**, 398 (2011).
 - [S4] F. Waßer, A. Schneidewind, Y. Sidis, S. Wurmehl, S. Aswartham, B. Büchner, and M. Braden, Phys. Rev. B **91**, 060505(R) (2015).
 - [S5] M. N. Gastiasoro and B. M. Andersen, Phys. Rev. B **92**, 150506(R) (2015).
 - [S6] K. Nakamura, R. Arita, and H. Ikeda, Phys. Rev. B **83**, 144512 (2011).
 - [S7] R. Wiesendanger, Rev. Mod. Phys. **81**, 1495 (2009).